

Large electromechanical strain and unconventional domain switching near phase convergence in a Pb-free ferroelectric

Sarangi Venkateshwarlu¹, Lalitha K. Venkataraman², Valentin Segouin^{3,4}, Frederick P. Marlton⁵, Ho Chin Hin¹, Dmitry Chernyshov^{6,7}, Yang Ren⁸, Mads R. V. Jørgensen^{5,9}, Sanjib Nayak¹, Jürgen Rödel², Laurent Daniel^{3,4} & Abhijit Pramanick¹✉

In many ferroelectrics, large electromechanical strains are observed near regions of composition- or temperature- driven phase coexistence. Phenomenologically, this is attributed to easy re-orientation of the polarization vector and/or phase transition, although their effects are highly convoluted and difficult to distinguish experimentally. Here, we used synchrotron X-ray scattering and digital image correlation to differentiate between the microscopic mechanisms leading to large electrostrains in an exemplary Pb-free piezoceramic Sn-doped barium calcium zirconate titanate. Large electrostrains of ~0.2% measured at room-temperature are attributed to an unconventional effect, wherein polarization switching is aided by a reversible phase transition near the tetragonal-orthorhombic phase boundary. Additionally, electrostrains of ~0.1% or more could be maintained from room temperature to 140 °C due to a succession of different microscopic mechanisms. In situ X-ray diffraction elucidates that while 90° domain reorientation is pertinent below the Curie temperature (T_C), isotropic distortion of polar clusters is the dominant mechanism above T_C .

¹Department of Materials Science and Engineering, City University of Hong Kong, Kowloon, Hong Kong SAR, China. ²Department of Materials and Earth Sciences, Technical University of Darmstadt, 64287 Darmstadt, Germany. ³Université Paris-Saclay, CentraleSupélec, CNRS, Laboratoire de Génie Electrique et Electronique de Paris, 91192 Gif-sur-Yvette, France. ⁴Sorbonne Université, CNRS, Laboratoire de Génie Electrique et Electronique de Paris, 75252 Paris, France. ⁵Center for Materials Crystallography, Department of Chemistry and iNANO, Aarhus University, 8000 Aarhus C, Denmark. ⁶SNBL, ESRF, 71 Avenue des Martyrs, Cedex 9, 38043 Grenoble, France. ⁷Peter the Great St. Petersburg Polytechnic University, St. Petersburg 195251, Russia. ⁸Advanced Photon Source, Argonne National Laboratory, Argonne, IL, USA. ⁹MAX IV Laboratory, Lund University, SE-221 00 Lund, Sweden. ✉email: apramani@cityu.edu.hk

Piezoelectrics exhibit high degrees of electromechanical coupling, providing large mechanical strains in response to electric fields or conversely large changes in electrical polarization in response to mechanical stress¹. Consequently, they are of interest for a broad array of applications including precision actuation, load sensing, telecommunications, biomedical imaging, and energy harvesting^{2–4}. The industrial applications for ferroelectrics as piezoceramics have been dominated by lead (Pb)-based compositions for over half a century. However, the search for new Pb-free alternatives has gained urgency in recent years due to toxicity of Pb and the impending worldwide regulations on the use of Pb in electronic materials^{5–9}. In this regard, Pb-free piezoceramics based on certain prototypical formulations, such as potassium sodium niobate (KNN), sodium bismuth titanate (NBT), and barium calcium zirconate titanate (BCZT), have gained attention. However, a recent study proposed that, in terms of detrimental environmental effects, KNN and NBT do not offer any advantages over lead zirconate titanate (PZT) or could even be worse¹⁰. Alternatively, interest in modified-BCMT (where M is a metal, such as Zr, Hf, or Sn) systems has seen a revival^{8,11}. The large electromechanical strains of BCMT, as defined by the converse piezoelectric coefficient $d_{33}^* = S/E$, where S is the induced strain under application of electric field E , also provides a competitive advantage to PZT for certain actuator applications^{8,11,12}. A purported shortcoming of BCMT ceramics is their relatively low T_C , although interestingly large electrostrains are noted for these materials several degrees above T_C ^{11–14}.

The most well studied among the BCMT systems is the (Ba,Ca)(Zr,Ti)O₃ or BCZT. The ternary phase diagram between BaTiO₃–BaZrO₃–CaTiO₃ was initially proposed by Ravez et al.¹⁵, based on which Liu and Ren later designed a pseudobinary solid solution of $(1-x)\text{Ba}(\text{Ti}_{0.8}\text{Zr}_{0.2})\text{O}_3-x(\text{Ba}_{0.7}\text{Ca}_{0.3})\text{TiO}_3$ or BZT- x BCT¹¹. Similar types of solid solutions were later designed for other BMT- x BCT systems, such as for $M = \text{Hf}, \text{Sn}$ ^{16,17}. A generic phase diagram of BMT- x BCT is illustrated in Fig. 1a, which characteristically exhibits temperature-dependent phase boundaries and a phase convergence region. Giant electromechanical responses are typically observed for compositions near phase boundaries, such as a $d_{33}^* \sim 1140 \text{ pm V}^{-1}$ have been reported for BZT- x BCT for $x = 0.5$ ¹¹, although the origin of which has not been unambiguously established. Ren and co-workers suggested that large electromechanical properties in BZT-BCT can be attributed to a vanishing polarization anisotropy near the rhombohedral(*R*)/tetragonal(*T*)/cubic(*C*) triple point, which aids easy polarization rotation and consequently large electromechanical susceptibility^{11,18}. This view was, however, challenged by later X-ray diffraction (XRD) and dielectric studies, which instead showed the occurrence of a polymorphic phase transition sequence similar to prototypical BaTiO₃ and existence of a four-phase convergence region^{13,19}. These studies attributed the large electromechanical properties near the phase convergence region to an elastic softening and phase instability within the orthorhombic (*O*) phase^{13,19}. Nevertheless, a comprehensive description of the microscopic mechanisms supporting either polarization rotation or the exact role of intermediate *O* phase is still missing. Although the possibility of significant contribution to electrostrain from *O* to *T* transition in conjunction with domain switching was discussed²⁰, direct evidence for the same has been absent.

From a materials design viewpoint, an interesting feature of the temperature-dependent properties of BCMT systems is that, although high electric field-induced polarization is indeed observed near the phase convergence region, the same is not true for electromechanical coefficients¹³. Instead, the maximum d_{33}^* is obtained near the *O*–*T* phase boundary (Fig. 1a)²⁰. This behavior

is rationalized based on the fact that the non-cubic lattice distortions are rather small near the phase convergence region^{13,14}. Therefore, while presumably easy polarization rotation and low energy barrier for polarization switching near the phase convergence region should aid towards large electromechanical susceptibility, this advantage is largely offset by the lower lattice distortions. Following this argument, in principle, introducing local lattice distortions for compositions close to the phase convergence region can result in larger electric field-induced strains. In this respect, some recent studies are noteworthy, wherein incorporation of Sn²⁺ at the A-site of BaTiO₃-based compositions was demonstrated to increase the tetragonality (*c/a*) of the crystal lattice^{21,22}, although the implication for the same on functional properties was not presented.

In this work, we examined the effect of Sn²⁺ substitution on the electrostrain properties of BCZT ((Ba_{0.95}Ca_{0.045}Sn_{0.005})(Ti_{0.875}Zr_{0.12}Sn_{0.005})O₃) ceramics near phase convergence region, which provided large d_{33}^* over a wider range of temperatures from room temperature (RT) to 140 °C as compared to undoped BCZT. Comprehensive insights into the microscopic origins of large electrostrains over a broader range of temperature were obtained from in situ XRD and digital image correlation (DIC) experiments. At RT, a reversible *T*–*O* phase transition is shown to initiate both 180° and 90° domain reorientation, which leads to large electrostrains at low fields. In contrast, electric field-induced strains at higher temperatures could be mostly attributed to conventional 90° domain reorientation and deformation of high temperature polar clusters. The transitory nature of the induced states observed here underpins the necessity of in situ diffraction experiments to clearly understand the microscopic mechanisms of new Pb-free piezoceramics. The results also address a long standing challenge, that of evaluating individual contributions to macroscopic electric field-induced strains from simultaneous phase transition and domain switching near phase boundaries^{23–25}.

Results

Dielectric and phase transition behavior. (Ba_{0.95}Ca_{0.045}Sn_{0.005})(Ti_{0.875}Zr_{0.12}Sn_{0.005})O₃ ceramics close to the phase convergence region¹⁹ but with broadened phase space of the *O* phase were selected for the current study. The temperature-dependent dielectric permittivity spectrum of the ceramic is displayed in Fig. 1b. A distinct peak near $T \sim 83 \text{ °C}$ marks the paraelectric to ferroelectric phase transition. Two additional anomalies at lower temperature were observed near $T \sim 20 \text{ °C}$ and $T \sim 0 \text{ °C}$. Figure 1c depicts the small-signal, converse d_{33}^* as a function of temperature, for which three clear inflection points are noted at 80, 33, and 0 °C and a broad anomaly at $\sim 55 \text{ °C}$.

To clearly understand the phase transition behavior, characterization of the structural changes was undertaken using high-resolution XRD of the powder samples at the Swiss–Norwegian beamline (SNBL) of the European Synchrotron Radiation Facility (ESRF). Phase transitions between the ferroelectric phases can be observed from the temperature-dependent changes in the pseudo-cubic 200 diffraction peak profile, as depicted in Fig. 1d. The peak profiles were fitted using a Pearson VII function and the extracted lattice parameters as a function of temperature are shown in Fig. 1e. The *c* and *a* lattice parameters in Fig. 1e are marked following the notation outlined in Jaffe and Jaffe¹, whereby the *O* phase is indexed as per the pseudomonoclinic unit cell for better comparison with the *R/T/C* phases. The temperature-dependent changes in the 002/200 peak profile for the current material is consistent with the following phase transition sequence: *C*-to-*T* at $T \sim 75 \text{ °C}$, *T*-to-*O* transition at $T \sim 20 \text{ °C}$ and *O*-to-*R* transition at $T \sim -25 \text{ °C}$, which has been

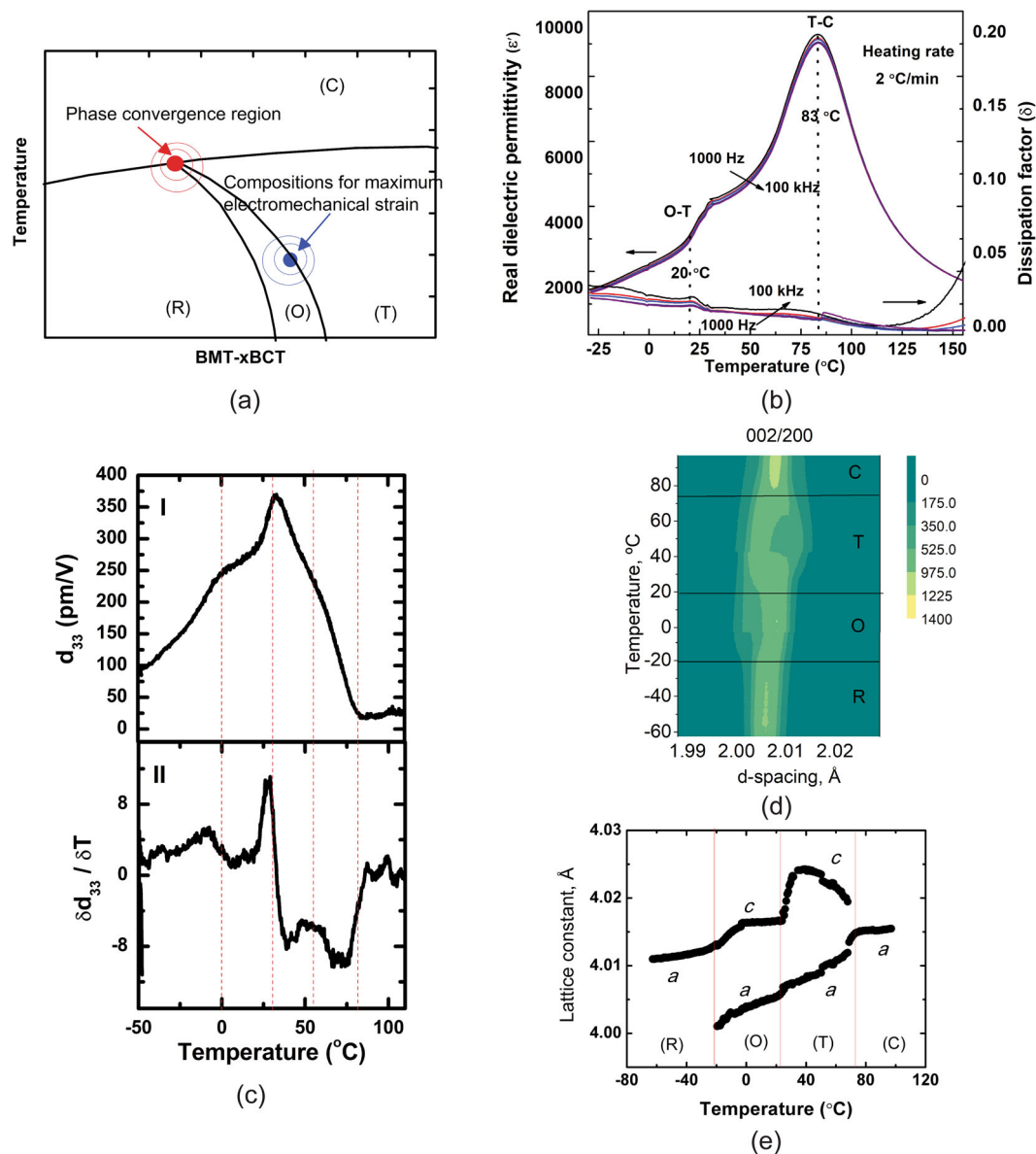


Fig. 1 Macroscopic properties and phase transition of Sn-doped (Ba,Ca)(Zr,Ti)O₃ (BCZT) ceramics. **a** Generic phase diagram of (Ba,Ca)(Ti,M)O₃ systems. The region in the phase space where all phases meet is marked in red. The largest electromechanical properties are instead observed near phase boundaries such as the orthorhombic/tetragonal (O/T) phase boundary region marked in blue. **b** Dielectric permittivity (ϵ') and dissipation factor ($\tan \delta$) of the Sn-doped BCZT composition studied here: (Ba_{0.95}Ca_{0.045}Sn_{0.005})(Ti_{0.875}Zr_{0.12}Sn_{0.005})O₃. **c** Small-signal piezoelectric coefficient d_{33} as a function of temperature (I). The $(\partial d_{33} / \partial T)$ plot, where T is temperature, shown in II indicates the location of the inflection points. **d** High-resolution X-ray diffraction peak profile of 002/200 peaks highlighting the crystallographic phase transitions from rhombohedral (R) to orthorhombic (O) to tetragonal (T) to cubic (C) at different temperatures. **e** The temperature-dependent changes in lattice parameters, a and c , obtained from fitting of the 002/200 diffraction peaks. For the orthorhombic (O) phase, in the monoclinic setting, angle β is close to 90°. The error bars for each data point were obtained based on fitting of the diffraction peaks; the errors were within the size of the data points.

reported for the undoped BCZT composition of (Ba_{0.85}Ca_{0.15})(Zr_{0.1}Ti_{0.9})O₃¹⁹. Further details about the temperature-dependent changes in other hkl diffraction peaks are provided in the Fig. S1 in Supplementary Information. These temperatures are close to the two of the three anomalies observed from the dielectric permittivity and d_{33} spectra. The inflection points for dielectric permittivity and small signal d_{33} curves at $T \sim 0^\circ$ do not correspond to any of the phase transitions points that are evident from XRD. A similar result was reported earlier by Haugen et al.²⁶. However, a change in slope of the temperature dependence of the lattice constant c is observed at $T \sim 0^\circ$ C, as depicted in Fig. 1e, which indicate subtle lattice distortions or

change in local atomic correlations. The most important observation is that the O-T transition is softer than the R-O and T-C transitions, as evident from the high d_{33} observed at this transition. This result is in accordance with the softening of the elastic compliance at the O-T transition for undoped BCZT²⁷. Modification by Sn doping therefore maintains the intrinsic nature of the elastic anomalies in BCZT ceramics.

Another interesting observation is a sharp increase in the lattice constant c near the O-T phase transition point. The sharp discontinuous change in lattice parameters near the O-T transition is similar to what is observed for prototypical BaTiO₃¹, but unlike a more continuous change described for the BCZT

ceramics near the phase convergence region²⁸. The sharp discontinuous change at the O - T transition for the Sn-doped BCZT ceramics likely reflects the strong lattice distortions introduced by Sn^{2+} doping at the A-site. The implication for such large lattice instability will be clearer from the discussion on the electric field-induced structural changes in the “Structural origins of temperature-dependent electric field-induced strains” section.

The broad anomaly observed for $(\partial d_{33}/\partial T)$ at $\sim 55^\circ\text{C}$ is not related to a crystallographic phase transition. However, this anomaly could be related to a non-linear expansion in unit cell volume (see Fig. S1e in Supplementary Information). In previous studies, such non-linear expansion in unit cell volume has been related to the formation of polar regions with short-range correlations²⁹, which requires further investigation.

Electric field-induced polarization and strain response. The polarization–electric field (P - E) and strain–electric field (S - E) loops at different temperatures from 20°C to 140°C are shown in Fig. 2a–c. The P - E loops depict features typical for ferroelectric materials. The coercive fields E_C are ~ 0.1 – 0.25 kV mm^{-1} in the temperature range of 20 – 120°C . A broadening of the P - E loop is observed at 140°C , which is due to an increase in conductivity of the sample. The corresponding S - E loops are non-linear from 20°C to 110°C , with a larger slope for $\partial S/\partial E$ below $E = 1\text{ kV mm}^{-1}$.

The maximum polarization (P_{max}) at different temperatures as obtained from analysis of the P - E loops is outlined in Fig. 2d. The corresponding values for electrostrain coefficients, $d_{33}^* = S/E$, for unipolar electric fields are plotted in Fig. 2e. Several interesting features could be noted. First, the P_{max} of Sn-doped BCZT ceramics is slightly higher than those reported for BCZT ceramics near the phase convergence regions, which probably reflects the additional local polar distortions introduced by the presence of Sn^{2+} at the A-site. Second, neither discontinuity in the temperature dependencies of P_{max} nor in d_{33}^* values is noticed across the phase transition temperatures, although large discontinuous changes in the lattice parameters and small-signal d_{33} are observed in the same region (Fig. 1c–e). Such behavior likely reflects low polarization anisotropy energy for this composition. Third, large P_{max} and d_{33}^* are observed above zero-field $T_C \sim 75^\circ\text{C}$ or the depolarization temperature of $\sim 80^\circ\text{C}$ as noted from the small-signal d_{33} measurements. It is known that application of electric field can shift the phase transition temperatures³⁰. Nevertheless, it is remarkable that a $d_{33}^* \sim 300\text{ pm V}^{-1}$ can be observed at $T = 120^\circ\text{C}$, which is 45°C higher than T_C . A notable feature is a gradual transition to an electrostrictive strain response above T_C , which is verified from Fig. 2f, which shows that the negative strain at E_C approaches zero above this temperature. The S - E loop exhibits mostly an electrostrictive response at 140°C . Fundamentally, observance of significant non-zero polarization and electrostrictive strain responses several degrees above T_C can be associated with local polar correlations linked to some precursor order, which is further elaborated in the “Structural origins of temperature-dependent electric field-induced strains” section. The microscopic origins of such electric field-induced strain responses for Sn-doped BCZT ceramics are characterized by in situ high-energy XRD experiments, supplemented by DIC, which are described below.

Structural origins of temperature-dependent electric field-induced strains. A schematic of the experimental setup for in situ XRD is displayed in Fig. 3a. Details of diffraction patterns measured at different azimuthal sectors are provided in Fig. S2 of Supplementary Information. Diffraction patterns were

recorded at different temperatures under stepwise changes of applied electric fields in the following sequence, as indicated in Fig. 3b: (A) the field was first increased to a maximum of 2 kV mm^{-1} in steps of 0.2 kV mm^{-1} , then decreased stepwise to zero (1st cycle) and (B) the electric field was then cycled in steps of 0.2 kV mm^{-1} between a maximum negative field of -2 kV mm^{-1} and a maximum positive field of 2 kV mm^{-1} (second cycle). The electric field-induced structural changes were monitored from the high symmetry peaks of 002/200 and 111, as further described below.

Electric field-induced structural changes at RT. Figure 3c, d shows contour plots of 002/200 peak intensities at RT for diffraction vectors approximately parallel to the electric field direction. The corresponding one-dimensional (1D) peak profiles are shown in Fig. 3e, f. The field-dependent changes in the 002/200 peak profiles are characteristically different for the first and the second cycles. For example, during the first cycle, the intensity of the 200 peak decreases with increasing electric field up to 2 kV mm^{-1} , while that of the 002 peak increases. However, during the second cycle the 002/200 peak profile undergoes a non-monotonic evolution. For example, with increasing electric field in the negative direction, up to -0.5 kV mm^{-1} , the intensity of the 002 peak increases, followed by a sharp decrease with increasing negative electric field to -1.0 kV mm^{-1} . Finally, the 002 peak intensity increases again for further stepwise negative increment in electric field to -2.0 kV mm^{-1} . The integrated peak intensity ratio I_{002}/I_{200} as a function of electric field is depicted in Fig. 3g. For perovskite ferroelectrics, I_{002}/I_{200} is expected to be ~ 0.5 for a randomly oriented distribution of 90° domains in the tetragonal (T) phase. For the orthorhombic (O) phase, a “monoclinic” unit cell with pseudotetragonal indices can be adopted as per ref. 1, for which $d_{001} = d_{100} > d_{010}$. Here, in order to be consistent with the tetragonal notation, the axes notations of the “monoclinic” unit cell for the O phase are modified to follow $d_{001} = d_{010} > d_{100}$, without any loss in generality. In this revised notation, based on multiplicity, I_{002}/I_{200} is expected to be ~ 2 in the orthorhombic (O) phase. For the current material, $I_{002}/I_{200} \sim 1.3$ at zero field in the unpoled state, which is likely due to an admixture of T and O phases. The arrows in Fig. 3g mark the progression of I_{002}/I_{200} with stepwise changes in electric field magnitude. During the first cycle, I_{002}/I_{200} mostly grows upon increase in applied electric field magnitude and vice versa. This is consistent with conventional 90° domain reorientation in tetragonal ferroelectric ceramics²³. However, as the electric field is cycled through negative and positive values during the second cycle, an unconventional behavior is observed. Remarkably, I_{002}/I_{200} first increases rapidly for change in field from zero to -0.5 kV mm^{-1} (marked as 1 in Fig. 3g), followed by an equally sharp decrease for further increment in field from -0.5 to -1 kV mm^{-1} (marked as 2 in Fig. 3g). A linear relationship is observed between electric field magnitude and I_{002}/I_{200} ratio for further increment in electric field to -2 kV mm^{-1} (marked as 3 in Fig. 3g). A similar linear relationship is observed when the electric field is decreased stepwise to 0 afterwards (marked as 4 in Fig. 3g). Identical behavior is repeated when the field direction is reversed and the electric field is cycled between 0 and 2 kV mm^{-1} (marked as 5–8 in Fig. 3g). A linear variation of I_{002}/I_{200} with electric field magnitude, as observed for electric field magnitudes $>1\text{ kV mm}^{-1}$, can be expected for conventional 90° domain reorientation in tetragonal ferroelectric ceramics³¹. However, the sharp variation in I_{002}/I_{200} at small field magnitudes ($<1\text{ kV mm}^{-1}$) is particularly intriguing since it features an inflection point at approximately $\pm 0.25\text{ kV mm}^{-1}$ and cannot be described by a conventional 90° domain reorientation phenomenon.

A possible rationalization for the sharp changes in diffraction peak intensities at low electric fields, such as demonstrated in

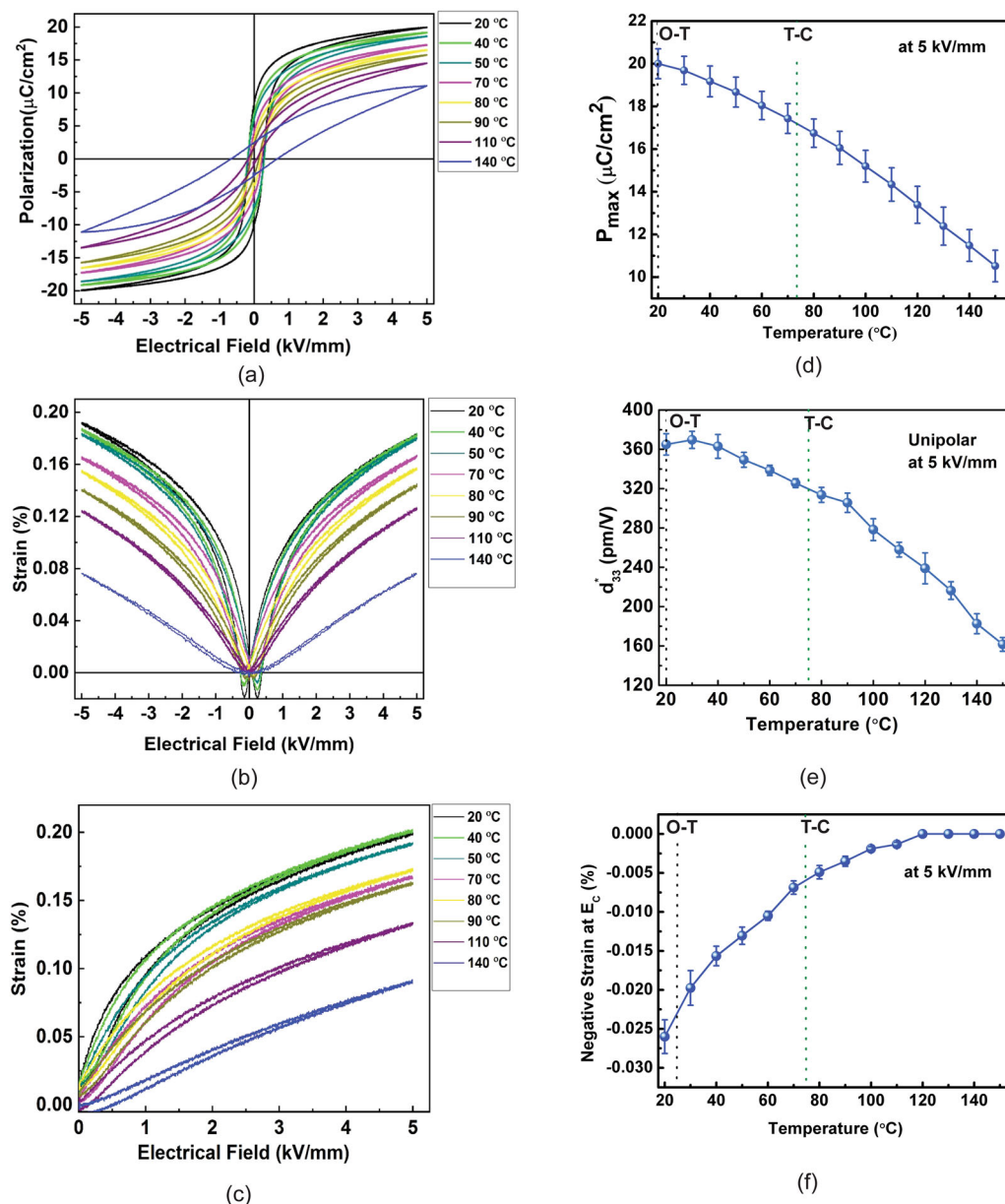


Fig. 2 Polarization and electromechanical strain of Sn-doped (Ba,Ca)(Zr,Ti)O₃ (BCZT) ceramics. **a** Polarization–electric field (P - E) loops measured at different temperatures. **b, c** Strain–electric field (S - E) loops measured at different temperatures for **b** bipolar and **c** unipolar fields. **d** Temperature-dependent maximum polarization P_{\max} obtained from P - E loops. **e** Temperature-dependent electrostrain coefficient $d_{33}^* = S_{\max}/E$ obtained from S - E loops measured for maximum field amplitude of 5 kV mm⁻¹ under unipolar fields. **f** Magnitudes of negative strain at coercive field E_c , which are obtained from the S - E loops shown in **b**. The error bars shown correspond to distribution of measured properties from multiple samples. In **d-f**, the dotted lines correspond to the boundaries between the respective phases, which are denoted by O (orthorhombic), T (tetragonal), and C (cubic).

Fig. 3g, can be an electric field-induced structural phase transition. In order to further investigate this possibility, we characterized the change in unit cell volume as a function of electric field. The unit cell volume is calculated from the factor $8 \times d_{(200)}^2 \times d_{(002)}$ (i.e. a^2c for nominal tetragonal unit cell) for the two sets of 90° domains, which have their polar 002 axis parallel and perpendicular to the electric field direction, respectively. As schematically illustrated in Fig. 4a, domains d1 have their 002 polar axis parallel to the electric field. Therefore, for d1, $d_{(002)}$ is obtained from the diffraction pattern measured at the azimuthal sector $\psi = 0^\circ$, whereas $d_{(200)}$ is obtained from the diffraction pattern measured at the azimuthal sector $\psi = 90^\circ$. Conversely, for domain d2 that has 002 polar axis perpendicular to the electric

field, $d_{(002)}$ is obtained from the diffraction pattern measured at the azimuthal sector $\psi = 90^\circ$, whereas $d_{(200)}$ is obtained from the diffraction pattern measured at the azimuthal sector $\psi = 0^\circ$. It is noted here that, in the current method, only a fraction of the domains with $d_{(002)}$ parallel to the field direction are sampled, since the ceramic is not rotated around the electric field direction. Nevertheless, as described below, distinct changes in lattice volume can be observed as a function of electric field magnitude.

The electric field-induced changes in $d_{(002)}$ and $d_{(200)}$ for domain d1 are featured in Fig. 4b. For clarity, $d_{(002)}$ and $d_{(200)}$ are plotted only for the sections of the second cycle constituting increasing magnitudes of the applied electric field. The plot should be read starting from zero field to a maximum negative

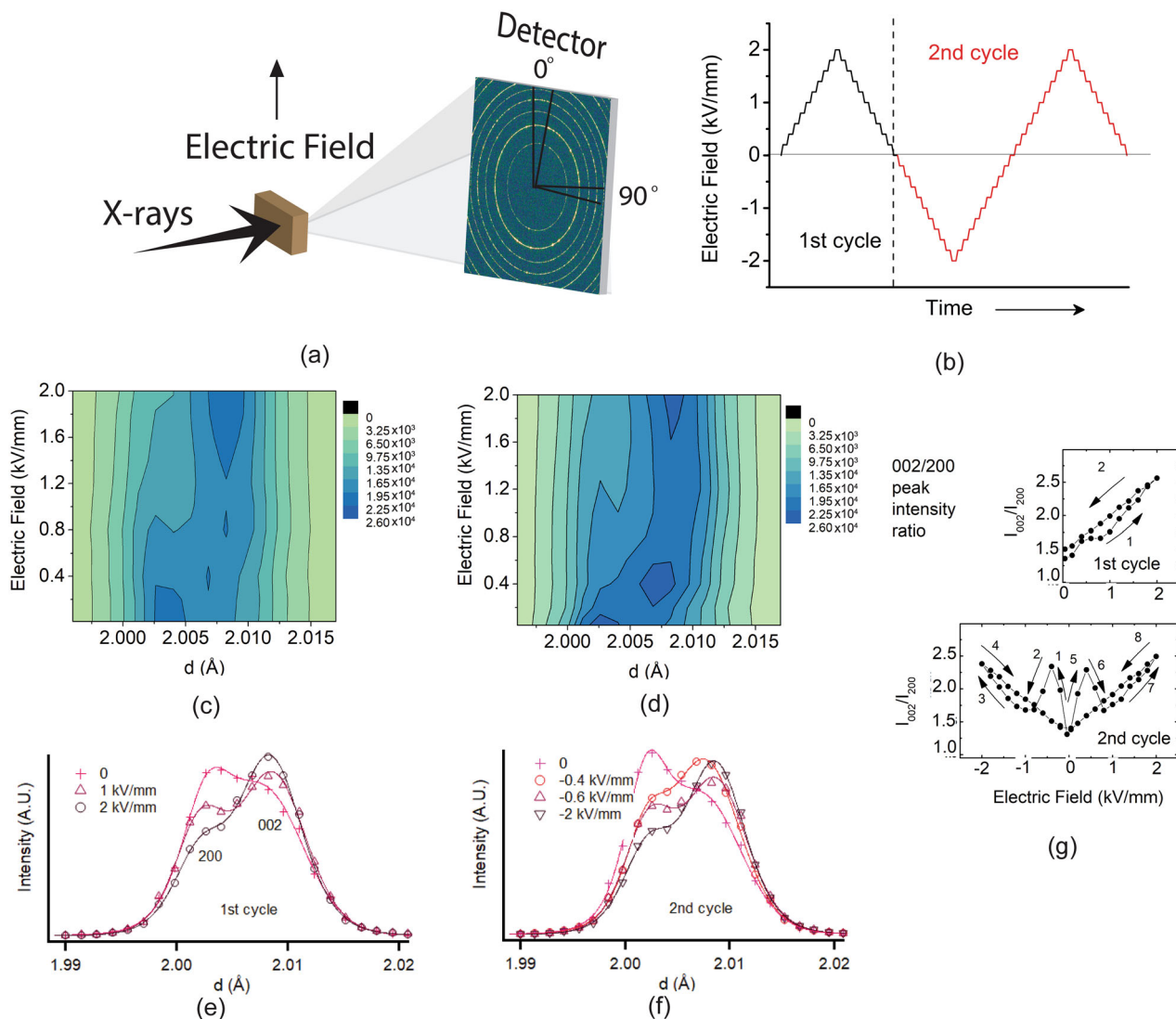


Fig. 3 Results of in situ X-ray diffraction experiments at room temperature. **a** Experimental set-up for in situ X-ray diffraction experiments under applied electric fields at different temperatures. **b** Schematic illustration of the applied electric field cycle for in situ diffraction experiments. **c, d** Contour plots of 002/200 peak intensities for different applied field magnitudes during the first (**c**) and second cycle (**d**) at room temperature. The color bar indicates measured diffraction intensity (arbitrary units). **e, f** The corresponding one-dimensional peak profiles during the first and second cycle at room temperature. All the data shown were measured during increasing electric field magnitude. In **c-f**, d represents lattice spacing. **g** Change in integrated peak intensity ratio I_{002}/I_{200} as a function of electric field magnitude. The arrows mark the progression of I_{002}/I_{200} with stepwise changes in electric field magnitude, while the numerals (1–8) mark the progressive segments of the plot. The error bars for each data point were obtained based on fitting of the diffraction peaks; the errors were within the size of the data points.

electric field of -2 kV mm^{-1} and then starting from zero field again to a maximum positive field of 2 kV mm^{-1} . It can be observed that $d_{(002)}$ (or $c/2$), while starting from a low value at 0.045 kV mm^{-1} , increases sharply for increasing negative electric field up to -1 kV mm^{-1} and then moderately decreases with further negative increment in electric field to -2 kV mm^{-1} . In comparison, $d_{(200)}$ (or $a/2$) rises for negative increment in electric field from 0.045 to -0.2 kV mm^{-1} , followed by a gradual decrease upon further negative increment in electric field up to -1 kV mm^{-1} and stabilizing thereafter. The changes in unit cell volume, a^2c , for domain d1 as a function of field magnitude is plotted in Fig. 4b. It demonstrates that the unit cell volume decreases initially when the polarity of the electric field is changed to negative after the first cycle. Subsequently, the unit cell volume increases for stepwise increment in electric field above E_C to -1

kV mm^{-1} and stabilizes thereafter. Nearly symmetrical trends are observed when the polarity of the electric field is changed to positive during the second part of the second cycle. Figure 4c provides the same information as in Fig. 4b, for domain d2. In this case, the unit cell volume is lowest for electric field magnitude of $\sim 0.75 \text{ kV mm}^{-1}$, as marked in Fig. 4c. Similar to d1, a decrease in lattice volume, a^2c , is followed by a subsequent increase; however, this phenomenon is noted at a higher absolute electric field magnitude of $\sim 0.75 \text{ kV mm}^{-1}$. In both cases, a decrease in lattice volume at intermediate field magnitudes, followed by an increase at larger fields, indicates an electric field-induced transient and reversible phase transition. The current results therefore emphasize the importance of investigating the microscopic strain contributions and changes in crystal structure using in situ XRD measurements with an area detector.

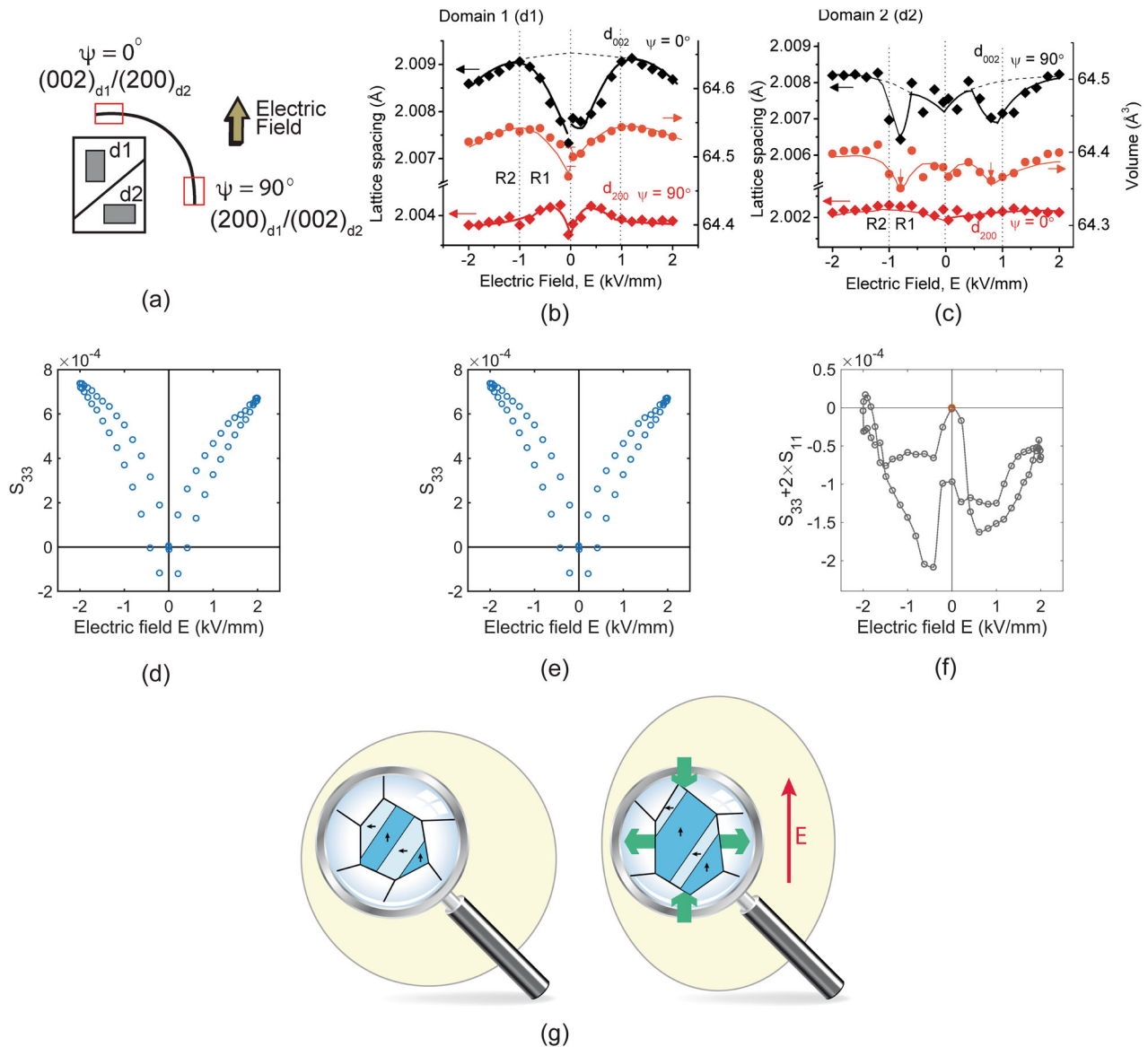


Fig. 4 Characterization of microscopic contributions to the macroscopic strain response at room temperature. **a** Schematic representation of the azimuthal sectors with respect to electric field direction, which are used to characterize the lattice spacings d_{002} and d_{200} for domains marked as d1 and d2. ψ represents the angle between direction of applied electric field and the wave vector for a particular azimuthal sector. **b, c** Electric field-induced changes in lattice spacings and unit cell volume of domains d1 and d2. In **b**, the starting point prior to first increment in negative (or positive) electric field is marked by red line; it indicates that the unit cell volume decreases even for a small magnitude of applied electric field. The dashed lines indicate the expected changes in lattice parameters due to internal stresses generated as result of 90° domain reorientation. Sharp deviations from the expected trend for field-dependent changes in lattice volume at intermediate field values indicate phase transition mechanism during which the total volume is not conserved. The different regimes for electric-field-induced structural changes are marked as R1, which is dominated by a reversible phase transition assisted domain reorientation process, and R2, which is dominated by 90° domain switching. The error bars for each data point were obtained based on fitting of the diffraction peaks; the errors were within the size of the data points. Non-conservation of material volume is also observed from macroscopic electrostrain measurements using digital imaging correlation (DIC) measurements. **d, e** Electric field-induced normal (S_{33}) and transverse (S_{11}) strain loops measured using DIC. **f** Large negative deviation in the factor $S_{33} + 2 \times S_{11}$ for electric fields $< 1 \text{ kV mm}^{-1}$ indicate non-conservation of total material volume. Details regarding error estimate for DIC measurements can be found in refs. ^{34,35}. The estimated error bars are comparable to the size of the data points. **g** Schematic illustration of internal stresses experienced by domains d1 and d2 during 90° domain reorientation process under applied electric field E . Domain d1 experiences compressive stress, while domain d2 experiences tensile stresses.

The X-ray measurements are complemented by DIC experiments³², which provides access to the transverse strain and volume change of the sample^{33,34}. The electric field-dependent normal strain (S_{33}) and the transverse strain (S_{11}) are depicted in Fig. 4d, e. For an applied electric field amplitude of 2 kV mm^{-1} , the mean strain values are $S_{33} = 7.7 \times 10^{-4}$ and $S_{11} = -4 \times 10^{-4}$. The corresponding values for electrostrain coefficients are $d_{33}^* =$

383 pm V^{-1} and $d_{31}^* = -195 \text{ pm V}^{-1}$. The absolute value of the shear component $|S_{31}|$ does not exceed 6% of the total S_{33} amplitude and is hence neglected. $S_{33} + 2S_{11}$ as a function of electric field magnitude are plotted in Fig. 4f. $S_{33} + 2S_{11}$ should be ideally zero for isovolumetric mechanisms such as 90° domain reorientation, although small deviations from a net zero value can occur due to internal stresses as a result of intergranular

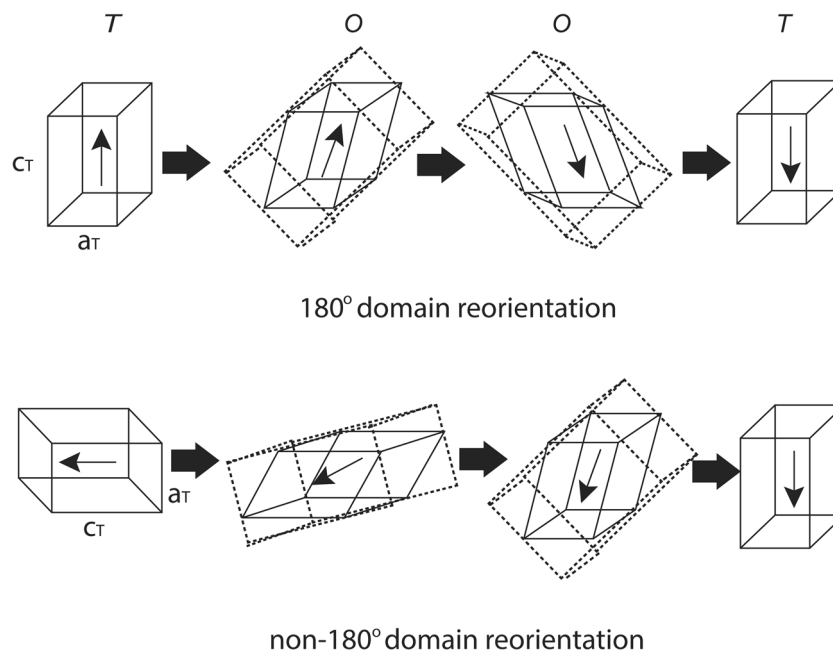


Fig. 5 Domain switching mechanism under applied electric field. Schematic illustration of the proposed 180° and 90° domain switching mechanism in tetragonal *T* phase, which proceeds through an intermediate orthorhombic *O* phase. a_T and c_T correspond to the dimensions of the tetragonal unit cell.

interactions³¹. Experimentally, two different regimes can be noted for field-dependent values of $S_{33} + 2S_{11}$ from Fig. 4f. For lower electric field values, one can observe large deviations from 0 for the factor $S_{33} + 2S_{11}$, which indicates that the volume of the specimen is not conserved. For field magnitudes $>1 \text{ kV mm}^{-1}$, $S_{33} + 2S_{11}$ yields a significantly smaller deviation from a zero value, while it approaches zero at maximum field magnitude. This observation is consistent with results of in situ XRD experiments, which indicated an electric field-induced phase transition at low electric fields, while 90° domain switching dominates for field magnitudes $>1 \text{ kV mm}^{-1}$.

In Fig. 4b, c, minimal changes in lattice volume are observed for electric field magnitudes $>1 \text{ kV mm}^{-1}$. This coincides with linear changes in the peak intensity ratio I_{002}/I_{200} in this field regime, as depicted in Fig. 3d, consistent with behavior expected for 90° domain reorientation. Interestingly, in this regime, one can observe a small decrease in d_{002} for domains d1 and small increase in d_{200} for domains d2. These changes in d_{002} can be expected due to internal stresses generated as a result of 90° domain reorientation, such as described in ref. 35. Specifically, due to intergranular stresses, the domains that have their polar 002 axis parallel to the electric field will experience a compressive stress, while domains that have their 002 axis perpendicular to the electric field will experience a tensile stress (Fig. 4g). The dotted lines in Fig. 4b, c indicate the expected changes in d_{002} for domains d1 and d2 as per this scenario. The changes in d_{002} generally coincide with the dotted lines for higher field magnitudes $>1 \text{ kV mm}^{-1}$ but deviates from the predicted trend for lower field magnitudes. The data for d2 show more scatter as compared to the data for d1, which could indicate effects from additional microstructural mechanisms, such as complex grain-to-grain interactions³¹.

Overall, a combined analysis of electric field-dependent changes in macroscopic polarization as well as both lattice parameter and I_{002}/I_{200} indicates two regimes for electric field-induced structural changes, as outlined in Fig. 4b, c: R1, which is dominated by a reversible phase transition-assisted domain reorientation process, and R2, which is dominated by 90° domain

switching. The proposed mechanism within the regime R1 is illustrated in Fig. 5. For domains d1, which have their initial polarization direction parallel to the electric field, it is proposed that, instead of a one-step process for 180° polarization switching at E_c , the polarization is first tilted in the *O* phase, followed by a flipping of the polarization direction (Fig. 5a). This is facilitated by the large elastic compliance of the lattice near the *T*-*O* phase transition point³². Similarly, for domains d2, which have their polarization direction perpendicular to the electric field, it is proposed that the polarization is first tilted in the *O* phase followed by a transition back to the *T* phase (Fig. 5b).

It is worth mentioning that the domain switching and phase transition mechanisms in the differently oriented grains are dependent on the orientation of their polarization vectors with respect to the electric field direction. The structural changes in the differently oriented grains can be ascertained by examining the changes in the profile of the other *hkl* peaks. While we have focussed here on the 002/200 peak profile changes, complementary information about electric field-dependent changes in the 111 peak profile is shown in Fig. S4 in Supplementary Information. A subtle splitting of the 111 peak in the orthorhombic (*O*) phase can be expected, such as shown in ref. 19. Although a clear splitting of the 111 peak was not apparent, we noted a significant change in the 111 peak width as a function of electric field magnitude (see Fig. S4 in Supplementary Information). Specifically, the peak width significantly decreases for field magnitudes $>1 \text{ kV mm}^{-1}$, which may indicate an *O*-to-*T* transition at $\sim 1 \text{ kV mm}^{-1}$. Therefore, similar to the 002-oriented grains, a structural transition is also noted for the grains with their 111 pole vectors parallel to the electric field, although the exact nature of the phase transition need to be resolved with higher-resolution measurements.

Electric field-induced structural changes at 50 °C. At 50 °C, the observed electric field-induced structural changes are characteristically different from those at RT, as depicted in Fig. 6a. Most importantly, unlike what is observed at RT, there are no sharp changes in I_{002}/I_{200} and d_{hkl} for field magnitudes below

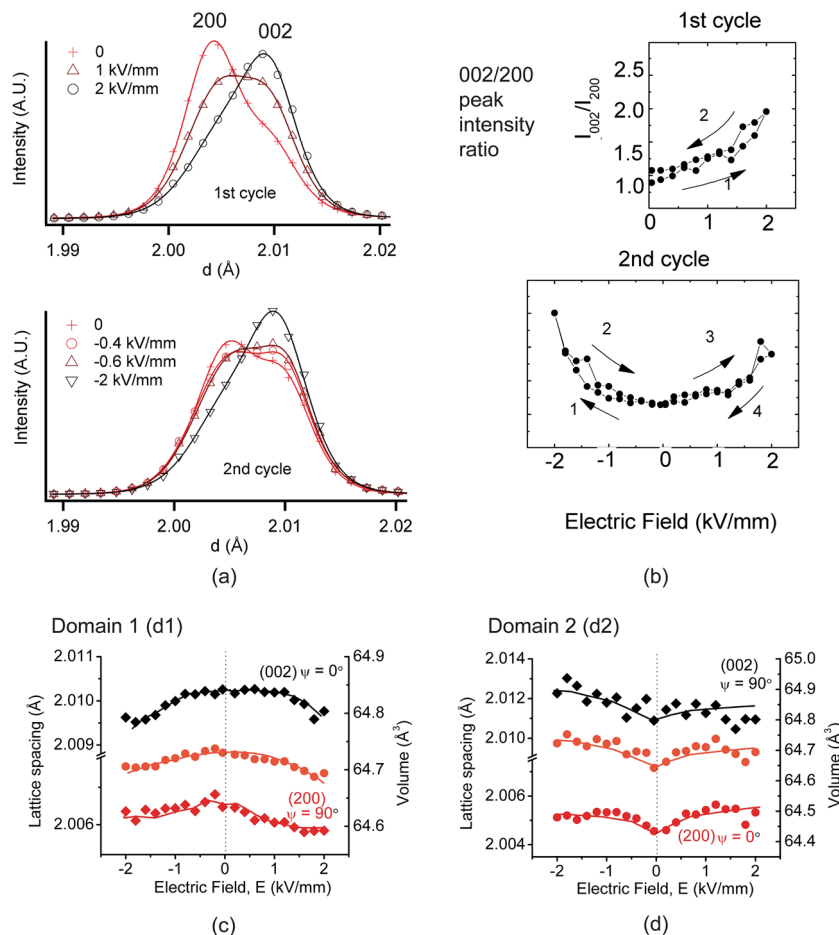


Fig. 6 Electric field-induced microstructural mechanisms at 50 °C. **a** 002/200 peak profiles for different applied field magnitudes during the first and second cycles at 50 °C. **b** Change in integrated peak intensity ratio I_{002}/I_{200} as a function of electric field magnitude. The arrows mark the progression of I_{002}/I_{200} with stepwise changes in electric field magnitude, while the numerals (1-4) mark the progressive segments of the plot. **c, d** Electric field-induced changes in lattice parameters and unit cell volume of domains d1 and d2. ψ represents the angle between direction of applied electric field and the wave vector for a particular azimuthal sector. Unlike room temperature, no sharp negative changes in unit cell volume can be observed at 50 °C. The error bars for each data point were obtained based on fitting of the diffraction peaks; the errors were within the size of the data points.

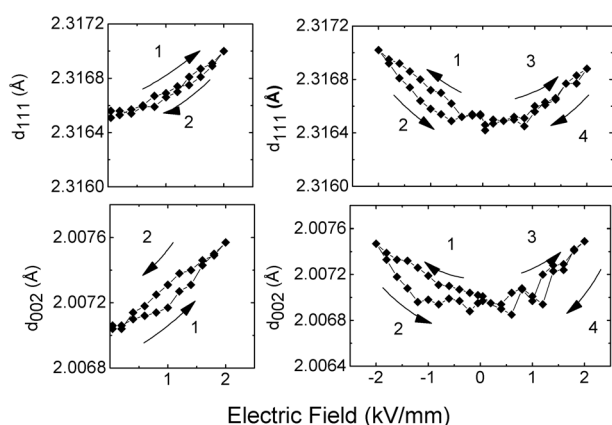


Fig. 7 Electric field-induced strain mechanism above Curie temperature **T_C**. Field-dependent changes in lattice spacing d_{111} and d_{002} indicate nearly isotropic lattice distortions for polar clusters above the Curie temperature T_C . The arrows mark the progression of I_{002}/I_{200} with stepwise changes in electric field magnitude, while the numerals (1-4) mark the progressive segments of the plot. The error bars for each data point were obtained based on fitting of the diffraction peaks; the errors were within the size of the data points.

1 kV mm⁻¹ (Fig. 6b). During both the first and second cycles, I_{002}/I_{200} monotonically changes with electric field magnitude (top panel), although the field dependence is not linear. The electric field-induced changes in I_{002}/I_{200} are more pronounced at field magnitudes >1 kV mm⁻¹. The bottom panel of Fig. 6b displays the field-induced changes in I_{002}/I_{200} , which similarly indicates monotonic but nonlinear variation as a function of electric field.

The electric field-dependent change in lattice volume at 50 °C is evaluated from d_{002} and d_{200} using the same procedure as described above. The results are displayed in Fig. 6c, d. Unlike the sharp deviations in lattice volume at intermediate fields as observed at RT, we observe monotonic variation as a function of field at 50 °C. The lack of sharp deviations in lattice volume indicates absence of any phase transition at this temperature. The variations in d_{002} and d_{200} also follow the trend as expected for a 90° domain reorientation process as described above.

Therefore, for temperatures where the material is away from the *O-T* phase boundary region and deep within the tetragonal (*T*) phase space, no electric field-induced phase transitions are observed. Instead, the electric field-induced strains can be mostly attributed to a domain reorientation process.

Electric field-induced structural changes at 100 °C. The in situ diffraction experiment at 100 °C provides succinct understanding

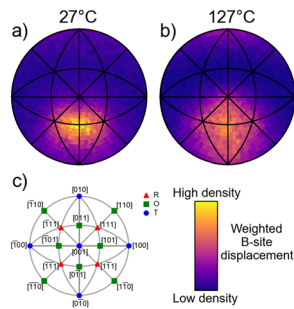
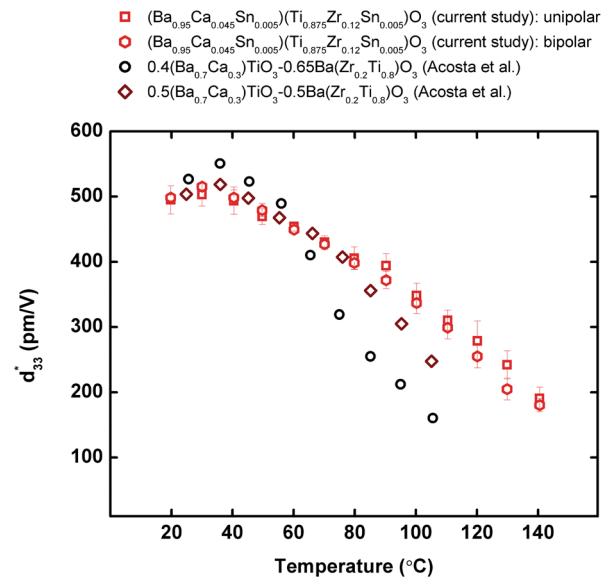


Fig. 8 Characteristics of atomic displacements in polar clusters.

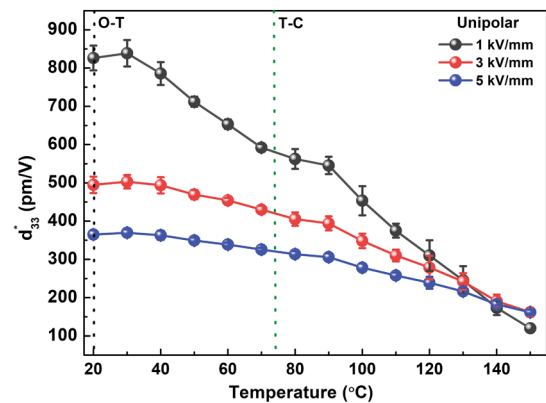
a, b Stereographic projections of atomic displacement directions of the B-site atoms viewed along [001] from the reverse Monte Carlo (RMC) analysis of X-ray total scattering data. **a, b** corresponds to data measured at 27 and 127 °C, respectively. The color bar on the right is used to indicate the weighted B-site displacements. **c** Schematic of the relevant symmetry-defining displacement directions in pseudo-cubic perovskites. The red, green, and blue markers correspond to the rhombohedral (R), orthorhombic (O), and tetragonal (T) displacement directions, respectively.

of the nature of electric field-induced structural mechanisms that contribute to the high-temperature electrostrain above $T_C \sim 75^\circ\text{C}$. The average structure of the material in this temperature regime is cubic. Figure 7 highlights the electric field-induced changes in d_{111} and d_{002} , which are similar for these high symmetry directions. Such isotropic nature of lattice strains can be expected for regions with local correlations between polar displacements that survive in an average cubic lattice above T_C ¹⁸. While the presence of local polar correlations has been alluded to in previous works^{18,36}, their exact microscopic nature has not been rationalized. Here, in order to obtain microscopic insights into the polar correlations at high temperature, the local atomic displacements were characterized by applying reverse Monte Carlo (RMC) analysis of X-ray total scattering pattern.

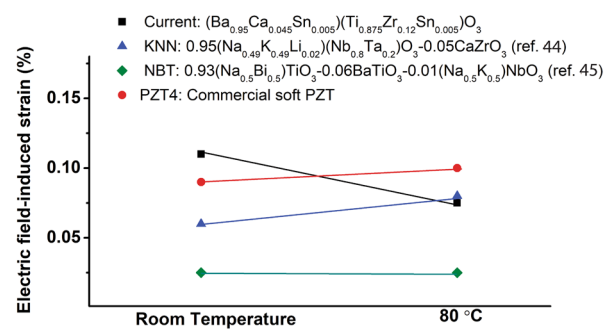
Figure 8a, b provides stereographic projections of local B-site displacements from the RMC modeling at 27 and 127 °C, respectively. The bright yellow regions of the contour plots are proportional to the density of B-site displacements weighted by their magnitude of displacement. The weighting was conducted in order to emphasize the directional displacements making a greater contribution to the local polarization. The displacements in the A-site were also investigated but yielded no significant trends (see Fig. S6 in Supplementary Information). Figure 8c features the stereographic projection with relevant symmetry-defining displacement directions that occur in pseudo-cubic perovskites. Figure 8a suggests that the displacements at 27 °C are close to an orthorhombic $0\bar{1}1$ direction. This is similar to the results obtained in ref. 22, which indicated that the local structure of Sn^{2+} -modified (Ba,Ca) TiO_3 is consistent with orthorhombic or tetragonal symmetry, although the spatially averaged structure appears cubic. There are also atomic displacements oriented along the line that connects the rhombohedral ($\langle 1\bar{1}1 \rangle$) and orthorhombic ($\langle 0\bar{1}1 \rangle$) directions on the stereographic projection, which corresponds to the monoclinic M_B phase^{37–40}. Such local displacements of B-site atoms could be responsible for facilitating the reversible phase transition observed at intermediate electric field values at RT, as it would allow for polarization rotation of the B-site atom from the [011] to [111] directions. This is reminiscent of model of continuous polarization rotation within the monoclinic phase described in some recent works, such as refs. 41,42. As described in Fig. 8b, the density of the displacements is much lower and more disordered at 127 °C but still clearly present. These high-temperature displacements are therefore deemed



(a)



(b)



(c)

Fig. 9 Temperature-dependent electromechanical properties.

a Comparison of the temperature-dependent electrostrain coefficient d_{33}^* of Sn-doped (Ba,Ca)(Zr,Ti) O_3 (BCZT) ceramics with those of undoped BCZT ceramics of different compositions at a maximum field of 3 kV mm^{-1} as compared to Acosta et al.⁴³ **b** Temperature dependence of electrostrain coefficient d_{33}^* as a function of applied maximum electric field. The dotted lines correspond to the boundaries between the respective phases, which are denoted by O (orthorhombic), T (tetragonal), and C (cubic). **c** Comparison of electric field-induced strain in different piezoceramics for applied electric field of 1 kV mm^{-1} , measured at room temperature and at 80°C ^{43,52,53}.

responsible for the high strain response exhibited by this material at elevated temperatures.

Discussion

Figure 9a provides a comparison of the temperature-dependent d_{33}^* of Sn-doped BCZT ceramics to those of the most commonly reported undoped $(1-x)\text{Ba}(\text{Ti}_{0.8}\text{Zr}_{0.2})\text{O}_3-x(\text{Ba}_{0.7}\text{Ca}_{0.3})\text{TiO}_3$ ceramics, such as in ref. 43. For the purpose of this comparison, two different compositions of $(1-x)\text{Ba}(\text{Ti}_{0.8}\text{Zr}_{0.2})\text{O}_3-x(\text{Ba}_{0.7}\text{Ca}_{0.3})\text{TiO}_3$ ceramics are chosen, which correspond to the phase convergence point ($x = 0.4$) and the O - T phase boundary ($x = 0.5$). Additionally, as shown in Fig. S7 in Supplementary Information, for identical Ba/Ca and Zr/Ti ratios, Sn doping leads to higher dielectric and electromechanical properties. The Sn-doped BCZT ceramics exhibit higher electrostrain coefficients as compared to undoped BCZT ceramics over a broader temperature range. A relatively high $d_{33}^* \sim 300 \text{ pm V}^{-1}$ at 120°C indicates improved thermal stability achieved with Sn doping for BCZT ceramics. The current results therefore suggest that, with suitable doping strategy, nominal doping of Sn at A (Sn^{2+}) and B (Sn^{4+}) sites, it is possible to enhance the temperature range of operation for BCMT-based solid solutions near the phase convergence region.

The microscopic origins of electric field-induced strain responses near the multiphase convergence point was revealed from in situ XRD experiments. While earlier works have alluded to the importance of O phase for large electromechanical properties of BCMT systems, the exact role played by the O phase had not been discussed. Here it is demonstrated that, close to the phase boundary between O and T phases, polarization rotation within an induced metastable O phase crucially assists domain switching at low electric fields. The large lattice distortions accompanying a reversible transition from O to T phase make significant contributions to macroscopic electric field-induced strains for field magnitudes $<1 \text{ kV mm}^{-1}$. As the temperature is increased to $\geq 50^\circ\text{C}$, an electric field-induced transition between O and T phases is absent; instead non- 180° domain switching is the main microscopic mechanism for electric field-induced strains. This has important implications for the temperature-dependent macroscopic strain response. $d_{33}^* = S/E$ decreases above 50°C for field magnitudes $<1 \text{ kV mm}^{-1}$, as can be observed from Fig. 9b. However, for higher field magnitudes, d_{33}^* exhibits less variation with temperature, since non- 180° switching becomes the principal contributing mechanism at high fields. Therefore, from a standpoint of material design, two aspects are apparent: first, the electric field-induced strain response in this material can be tuned by choosing appropriate field amplitudes so as to obtain either large strain response over narrow temperature range or a more moderate strain response over a broader temperature range. Second, for many actuator applications, large strains are required at low field amplitudes ($<1 \text{ kV mm}^{-1}$). Therefore, it will be desirable to benchmark the performance of the current material with respect to that of other Pb-based and Pb-free materials. Such a comparison is provided in Fig. 9c, which includes representative data for maximum strain at 1 kV mm^{-1} at RT and 80°C for different ceramic compositions. The current material exhibits higher strain as compared to other Pb-free materials at field amplitudes $<1 \text{ kV mm}^{-1}$, while maintaining comparable strain performance with commercial PZT at 80°C , which makes it attractive for actuator applications. To further expand the temperature range, it will be desirable that BCMT systems sustain reversible transitions between O and T phases over broader temperature range by, for example, designing a more diffuse O/T phase boundary.

Another noteworthy feature of the current material, and in general for BCMT systems, is the large electric field-induced

polarization and strain above $T_C \sim 75^\circ\text{C}$, where the material is nominally in the paraelectric cubic phase. In the previous section, it was demonstrated that large electrostrains above T_C in the current material derive from an isotropic deformation of regions with short-range polar correlations, which are formed as a result of locally correlated B-site atomic displacements. It therefore demonstrates that, while BCMT systems may have relatively low T_C , large electric field-induced strains at higher temperatures can in fact be sustained by improving the stability of locally correlated polar displacements above T_C using different doping strategies. In this regard, it will be important to examine the temporal stability of local atomic displacements using methods such as dynamic pair distribution function (Dy PDF)⁴⁴.

Methods

Sample preparation. $(\text{Ba}_{0.95}\text{Ca}_{0.045}\text{Sn}_{0.005})(\text{Ti}_{0.875}\text{Zr}_{0.12}\text{Sn}_{0.005})\text{O}_3$ polycrystalline ceramics were prepared by the conventional solid state method. High purity BaCO_3 (99.5%), CaCO_3 (99%), SnO_2 (99.8%), TiO_2 (99%), and ZrO_2 (99.9%) powders were weighed in desired stoichiometric amounts and ball milled for 24 h at 300 rpm in ethanol using zirconia grinding media. Following this, the slurry was dried at 100°C for 12 h and subsequently calcined at 1350°C for 6 h with heating/cooling rate of $10^\circ\text{C min}^{-1}$. The calcined powder was then ball milled for 24 h in ethanol and the slurry was again dried at 100°C for 12 h. Subsequently, the final synthesized powder was ground, mixed with polyvinyl alcohol, sieved, and pressed into pellets of 10 mm diameter and $\sim 1 \text{ mm}$ thickness using a uniaxial press (14 MPa). The green bodies were sintered at 1450°C with a heating rate $10^\circ\text{C min}^{-1}$ for 4 h in ambient atmosphere. Further, the ceramics were annealed under reducing oxygen partial pressure ($p\text{O}_2$) environment at 10^{-3} Pa at 1100°C for 20 h, and afterwards, the ceramics were annealed at 1000°C for 10 h in ambient atmosphere. The co-existence of Sn^{2+} and Sn^{4+} of the Sn-doped BCST composition is confirmed by X-ray photoelectron spectroscopic analysis (see Fig. S8 in Supplementary Information). The sintered samples were polished and painted with electrodes. For electrodes, silver paste was painted on the surface and burnt-in at 130°C for 1 h. The density of all compositions was determined using the Archimedes method and relative density is about 94%.

Measurement of electrical and electromechanical properties. The real (ϵ') and imaginary (ϵ'') dielectric relative permittivity of the unpoled ceramics were measured by an LCR meter (Agilent-4284A, Technologies Inc., Santa Clara, CA) in the range from -50°C to 200°C , with a heating rate of 2°C min^{-1} , and in the frequency range from 100 Hz to 100 kHz. Four different samples of the same composition of the ceramic were chosen for polarization (P - E) and electromechanical measurements (S - E). Prior to P - E and S - E loop measurements as well as small signal (d_{33}) quantification, the samples were poled under an electric field of 5 kV mm^{-1} for 15 min at 25°C . After 24 h aging of the poled samples, the poling state was monitored by obtaining d_{33} value using a Berlincourt meter. The average direct piezoelectric coefficient (d_{33}) of the four samples is about $\sim 380 \text{ pC N}^{-1}$ at 25°C . Small-signal (d_{33}) and large-signal (d_{33}^*) electromechanical responses and polarization-electrical field measurements were taken from all four samples. The values reported for the different property coefficients are average of those measured from all four samples.

Small-signal d_{33} was measured in situ in the temperature range -50°C to 150°C . The displacement was measured in a custom-designed device using a laser vibrometer (Polytec VDD-E-600 and a Polytec OFV-505 sensor head)⁴⁵ with an applied voltage of 10 V at 1 kHz and a heating rate of 2°C min^{-1} . Large-signal strain and polarization as functions of temperature were obtained using a commercial piezoelectric system using a TREK high voltage amplifier (Model 20/20 C, BFi OPTILAS GmbH, Germany). Large-signal strain and polarization measurement were carried out with a bipolar, triangular electric field of 5 kV mm^{-1} at 1 Hz in the range from 20 to 140°C . Application of the high-voltage amplitude (5 kV mm^{-1}) was chosen purposefully to ensure complete saturation of the polarization-electric field hysteresis loop of the ceramic.

XRD experiments

Temperature-dependent high-resolution synchrotron powder diffraction. High-resolution XRD measurement of powder samples of Sn-doped BCZT were carried out at the SNBL of the ESRF⁴⁶. The wavelength used for these measurements was 0.95 \AA . Diffraction patterns were collected in the range of temperature of -60°C to 150°C . An Oxford Cryosystem was used to control the temperature of the sample for temperature-dependent diffraction measurements.

In situ diffraction under applied electric fields. A rectangular ceramic sample of dimensions $1 \text{ mm} \times 1 \text{ mm} \times 5 \text{ mm}$ was used for in situ XRD experiments at the Sector 11-ID of the Advanced Photon Source (APS) at the Argonne National Laboratory. The experimental set-up is schematically illustrated in Fig. 3a. The temperature of the sample was varied using a pre-calibrated Oxford Cryosystem.

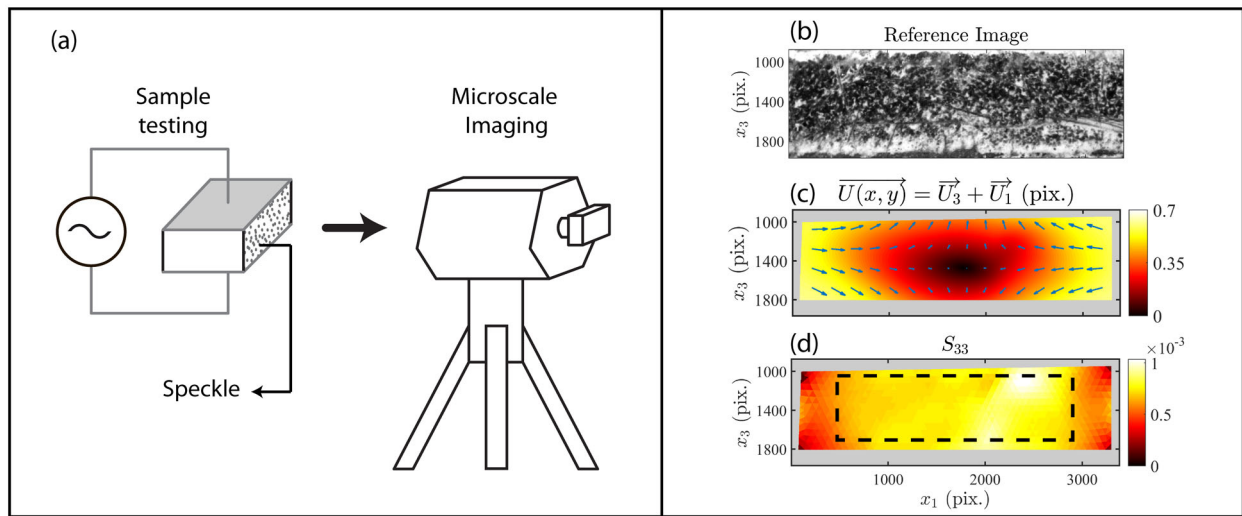


Fig. 10 Experimental set-up and image analysis of digital image correlation (DIC) experiments. **a** Schematic of the experimental set-up for digital imaging correlation (DIC) measurements. x_1 and x_3 correspond to the coordinates of the pixels (pix.) along axes 1 and 3, respectively. **b** Reference image of the sample taken before application of electric field E . **c**, **d** The displacement field (U) and the longitudinal strain field S_{33} obtained at $E = 2 \text{ kV mm}^{-1}$. The color bar represents the magnitude of the strain field U (no units).

The wavelength used for these measurements was 0.1173 \AA . Because of the high energy of the incident X-rays, the diffraction patterns were collected in the transmission mode and the wave vectors for the measured pattern are approximately perpendicular to the incident X-ray beam direction. 1D peak profiles were obtained from the diffraction images using the software Fit2D⁴⁷. Diffraction peak profiles were then quantitatively analyzed using custom written code in IGORPro. Details of peak fitting are provided in Fig. S3 in Supplementary Information.

X-ray total scattering measurements. Variable temperature X-ray total scattering patterns were collected at beamline ID22, ESRF. Samples were packed into 0.7 mm borosilicate capillaries and an Oxford Cryosystems was employed for temperature control. The wavelength λ of the X-rays was $0.1907122(5) \text{ \AA}$ with collection times 125 s (sum of 250 exposures of 0.5 s). Two-dimensional diffraction data were obtained on a flat panel Perkin Elmer XRD 1611CP3 with a pixel size of $100 \times 100 \mu\text{m}^2$, which was calibrated using a LaB_6 standard and converted to 1D data using the software Dioptas⁴⁸. The total scattering function and PDF were calculated using the software package XPDFsuite⁴⁹, with a \mathbf{Q}_{max} ($\mathbf{Q} = 4\pi\sin\theta/\lambda$) of 18 \AA^{-1} .

The RMC modeling was conducted using the software package RMCProfile⁵⁰. The unit cell parameters determined from Rietveld refinement of the XRD pattern were obtained in the software Topas⁵¹ and used to construct a $12 \times 12 \times 12$ supercell. The refinement was conducted against the PDF, total scattering function $F(\mathbf{Q})$ and the Bragg profile. Distance-window constraints and bond valence sum restraints were applied to prevent unphysical moves from occurring. The atom swapping function was applied for the mixed valence atoms on the A- and B-sites. To improve the statistics, the refinements were conducted a total of 20 times from the same starting configuration, which were subsequently combined for the analysis. Details of the fitting of the Bragg diffraction pattern, $F(\mathbf{Q})$ data, and PDF data are provided in Fig. S5 in Supplementary Information.

The stereographic projection of the atomic displacements was determined from all atoms of a particular site in the supercell in order to get a full representation of the model. Atoms with a negative $[001]_{\text{pc}}$ were inverted through the origin as only one hemisphere of the stereographic projection can be displayed. From here, the directions of the atomic displacements were binned in 5° angular steps ($\pm 2.5^\circ$ from the center of direction with respect to both the $[001]$ and $[100]$ directions) and weighted by their magnitude of displacement to generate a weighted histogram, which is plotted on the stereogram. When assessing the directional magnitude of displacement, the weighted bins were divided by unweighted bins to give the average magnitude of displacement within 5° angular ranges.

DIC spectroscopic measurements. The orientation-dependent electric field-induced strain response at RT was obtained using DIC measurements³². The detailed description of the experimental methodology for image collection and analysis for DIC with reference to electrostrain measurements can be found in refs. 33,34. A lateral face of the sample is first prepared by painting a random speckle (see Fig. 10a). A reference image is then taken at zero field (see Fig. 10b). For each electric field level E , a new picture is taken, and the in-plane displacement field is obtained by correlating this new image with the reference image. The strain field (components S_{33} , S_{11} , and S_{31}) is numerically evaluated from the displacement field. Several images are obtained during the electrical loading of the sample (sine waveform, amplitude of 2 kV mm^{-1} , frequency of 80 mHz). As an example,

Fig. 10c, d, respectively, display the displacement field and the longitudinal strain field S_{33} obtained at $E = 2 \text{ kV mm}^{-1}$. The S - E loops (Fig. 4d, e) are further obtained by plotting the average strain field as a function of electric field. The average is made using the elements inside the black dashed rectangle (Fig. 10d). The data outside the rectangle is discarded since the correlation is affected by edge effects (discontinuity of the displacement field), leading to an inhomogeneous strain.

Data availability

All relevant data are available from the corresponding author upon reasonable request.

Received: 29 March 2020; Accepted: 29 September 2020;

Published online: 30 October 2020

References

- Jaffe, B., Cook, W. R. & Jaffe, H. L. *Piezoelectric Ceramics* (Academic Press, Cambridge, 1971).
- Wersing, W. in *Piezoelectric Materials in Devices* (ed. Setter, N.) 29–66 (Ceramics Laboratory, EPFL, 2002).
- Uchino, K. *Ferroelectric Devices* (Marcel Dekker, Inc., New York, 2000).
- Bowen, C. R., Kim, H. A., Weaver, P. M. & Dunn, S. Piezoelectric and ferroelectric materials and structures for energy harvesting applications. *Energy Environ. Sci.* **7**, 25–44 (2014).
- Rödel, J. & Li, J.-F. Lead-free piezoceramics: status and perspectives. *MRS Bull.* **43**, 576–580 (2018).
- Bell, A. J. & Deubzer, O. Lead-free piezoceramics – the environmental and regulatory issues. *MRS Bull.* **43**, 581–587 (2018).
- Rödel, J. et al. Transferring lead-free piezoelectric ceramics into applications. *J. Eur. Ceram. Soc.* **35**, 1659 (2015).
- Acosta, M. et al. BaTiO₃-based piezoelectrics: fundamentals, current status and perspectives. *App. Phys. Rev.* **4**, 041305 (2017).
- Acosta, M. et al. Cytotoxicity, chemical stability, and surface properties of ferroelectric ceramics for biomaterials. *J. Am. Ceram. Soc.* **101**, 440–449 (2018).
- Ibn-Mohammed et al. Life cycle assessment and environmental profile evaluation of lead-free piezoelectrics in comparison with lead zirconate titanate. *J. Eur. Ceram. Soc.* **38**, 4922–4938 (2018).
- Liu, W. & Ren, X. Large piezoelectric effect in Pb-free ceramics. *Phys. Rev. Lett.* **103**, 257602 (2009).
- Gao, J., Ke, X., Acosta, M., Glaum, J. & Ren, X. High piezoelectricity by multiphase coexisting point: barium titanate derivatives. *MRS Bull.* **43**, 595–599 (2018).
- Acosta, M., Novak, N., Jo, W. & Rödel, J. Relationship between electromechanical properties and phase diagram in the $\text{Ba}(\text{Zr}_{0.2}\text{Ti}_{0.8})\text{O}_{3-x}$ ($\text{Ba}_{0.7}\text{Ca}_{0.3}$)TiO₃ lead-free piezoceramic. *Acta Mater.* **80**, 48–55 (2014).

14. Acosta, M. et al. Origin of large piezoelectric activity in $(1-x)\text{Ba}(\text{Zr}_{0.2}\text{Ti}_{0.8})\text{O}_{3-x}(\text{Ba}_{0.7}\text{Ca}_{0.3})\text{TiO}_3$ ceramics. *Phys. Rev. B* **91**, 104108 (2015).
15. Ravez, J. & Simon, A. Some solid state chemistry aspects of lead-free relaxor ferroelectrics. *J. Solid State Chem.* **162**, 260–265 (2001).
16. Xue, D. et al. Large piezoelectric effect in Pb-free $\text{Ba}(\text{Ti},\text{Sn})\text{O}_{3-x}(\text{Ba},\text{Ca})\text{TiO}_3$ ceramics. *Appl. Phys. Lett.* **99**, 122901 (2011).
17. Zhou, C. et al. Triple-point-type morphotropic phase boundary based large piezoelectric Pb-free material- $\text{Ba}(\text{Ti}_{0.8}\text{Hf}_{0.2})\text{O}_3-(\text{Ba}_{0.7}\text{Ca}_{0.3})\text{TiO}_3$. *Appl. Phys. Lett.* **100**, 222910 (2012).
18. Gao, J. et al. Phase transition behaviours near the triple point for Pb-free $(1-x)\text{Ba}(\text{Zr}_{0.2}\text{Ti}_{0.8})\text{O}_{3-x}(\text{Ba}_{0.7}\text{Ca}_{0.3})\text{TiO}_3$ piezoceramics. *EPL* **115**, 37001 (2016).
19. Keeble, D. S., Benabdallah, F., Thomas, P. A., Maglione, M. & Kreisel, J. Revised structural phase diagram of $\text{Ba}(\text{Zr}_{0.2}\text{Ti}_{0.8})\text{O}_{3-x}(\text{Ba}_{0.7}\text{Ca}_{0.3})\text{TiO}_3$. *Appl. Phys. Lett.* **102**, 092903 (2013).
20. Acosta, M., Novak, N., Rossetti, Jr, G. A., Rödel, J. Mechanisms of electromechanical response in $(1-x)\text{Ba}(\text{Zr}_{0.2}\text{Ti}_{0.8})\text{O}_{3-x}(\text{Ba}_{0.7}\text{Ca}_{0.3})\text{TiO}_3$ ceramics. *Appl. Phys. Lett.* **107**, 142906 (2015).
21. Suzuki, S. et al. Substitution of Sn ions in $(\text{Ba},\text{Ca})\text{TiO}_3$ perovskites. *Jpn. J. Appl. Phys.* **51**, 09LC08 (2012).
22. Laurita, G., Page, K., Suzuki, S. & Seshadri, R. Average and local structure of the Pb-free ferroelectric perovskites $(\text{Sr},\text{Sn})\text{TiO}_3$ and $(\text{Ba},\text{Ca},\text{Sn})\text{TiO}_3$. *Phys. Rev. B* **92**, 214109 (2015).
23. Schönau, K. A., Knapp, M., Kungl, H., Hoffmann, M. J. & Fuess, H. In situ synchrotron diffraction investigation of morphotropic $\text{Pb}(\text{Zr}_{1-x}\text{Ti}_x)\text{O}_3$ under an applied electric field. *Phys. Rev. B* **76**, 144112 (2007).
24. Ma, C., Guo, H., Beckman, S. P. & Tan, X. Creation and destruction of morphotropic phase boundaries through electrical poling: a case study of lead-free $(\text{Bi}_{1/2}\text{Na}_{1/2})\text{TiO}_3\text{-BaTiO}_3$ piezoelectrics. *Phys. Rev. Lett.* **109**, 107602 (2012).
25. Ehmke, M. C., Ehrlich, S. N., Blendell, J. E. & Bowman, K. J. Phase coexistence and ferroelectric texture in high strain $(1-x)\text{Ba}(\text{Zr}_{0.2}\text{Ti}_{0.8})\text{O}_{3-x}(\text{Ba}_{0.7}\text{Ca}_{0.3})\text{TiO}_3$ piezoceramics. *J. Appl. Phys.* **111**, 124110 (2012).
26. Haugen, A. B. et al. Structure and phase transitions in $0.5(\text{Ba}_{0.7}\text{Ca}_{0.3})\text{TiO}_3\text{-}0.5(\text{BaZr}_{0.2}\text{Ti}_{0.8}\text{O}_3)$ from -100°C to 150°C . *J. Appl. Phys.* **113**, 014103 (2013).
27. Cordero, F. et al. Elastic response of $(1-x)\text{Ba}(\text{Ti}_{0.8}\text{Zr}_{0.2})\text{O}_{3-x}(\text{Ba}_{0.7}\text{Ca}_{0.3})\text{TiO}_3$ ($x=0.45\text{-}0.55$) and the role of the intermediate orthorhombic phase in enhancing the piezoelectric coupling. *Appl. Phys. Lett.* **105**, 232904 (2014).
28. Kalyani, A. J., Senyshyn, A. & Ranjan, R. Polymorphic phase boundaries and enhanced piezoelectric response in extended composition range in the lead free ferroelectric $\text{BaTi}_{1-x}\text{Zr}_x\text{O}_3$. *J. Appl. Phys.* **114**, 014102 (2013).
29. Gehring, P. M. et al. Reassessment of the Burns temperature and its relationship to diffuse scattering, lattice dynamics, and thermal expansion in relaxor $\text{Pb}(\text{Mg}_{1/3}\text{Nb}_{2/3})\text{O}_3$. *Phys. Rev. B* **79**, 224109 (2009).
30. Sapper, E., Novak, N., Jo, W., Granzow, T. & Rödel, J. Electric-field-temperature phase diagram of the ferroelectric relaxor system $(1-x)\text{Bi}_{1/2}\text{Na}_{1/2}\text{TiO}_3\text{-}x\text{BaTiO}_3$ doped with manganese. *J. Appl. Phys.* **115**, 194104 (2014).
31. Pramanick, A., Daniels, J. E., Damjanovic, D., Nino, J. C. & Jones, J. L. Origins of electro-mechanical coupling in polycrystalline ferroelectrics during subcoercive electrical loading. *J. Am. Ceram. Soc.* **94**, 293–309 (2011).
32. Tomicevc, Z., Hild, F. & Roux, S. Mechanics-aided digital image correlation. *J. Strain Anal. Eng. Des.* **48**, 330–343 (2013).
33. Segouin, V., Domenjoud, M., Bernard, Y. & Daniel, L. Development of a 2D DIC experimental tool for piezoelectric strains measurements. In *Proc. Society for Experimental Mechanics Series, 200869* 45–50 (Springer International Publishing, 2016).
34. Segouin, V., Domenjoud, M., Bernard, Y. & Daniel, L. Mechanics-aided digital image correlation for the investigation of piezoelectric and ferroelectric behavior of a soft PZT. *J. Eur. Ceram. Soc.* **39**, 2091–2102 (2019).
35. Daniel, L. et al. Revisiting the blocking force test on ferroelectric ceramics using high energy x-ray diffraction. *J. Appl. Phys.* **117**, 174104 (2015).
36. Damjanovic, D., Biancoli, A., Batooli, L., Vahabzadeh, A. & Trodahl, J. Elastic, dielectric, and piezoelectric anomalies and Raman spectroscopy of $0.5\text{Ba}(\text{Ti}_{0.8}\text{Zr}_{0.2})\text{O}_3\text{-}0.5(\text{Ba}_{0.7}\text{Ca}_{0.3})\text{TiO}_3$. *Appl. Phys. Lett.* **100**, 192907 (2012).
37. Zhang, N. et al. The missing boundary in the phase diagram of $\text{PbZr}_{1-x}\text{Ti}_x\text{O}_3$. *Nat. Commun.* **5**, 5231 (2014).
38. Zhao, C., Li, F., Zhang, S., Li, S. & Jones, J. L. Mechanisms underpinning the ultrahigh piezoelectricity in Sm-doped $0.705\text{Pb}(\text{Mg}_{1/3}\text{Nb}_{2/3})\text{O}_3\text{-}0.295\text{PbTiO}_3$. *J. Appl. Phys.* **126**, 075101 (2019).
39. Noheda, B. & Cox, D. E. Bridging phases at the morphotropic boundaries of lead oxide solid solutions. *Phase Transit.* **79**, 5–20 (2006).
40. Vanderbilt, D. & Cohen, M. H. Monoclinic and triclinic phases in higher-order Devonshire theory. *Phys. Rev. B* **63**, 094108 (2001).
41. Liu, H. et al. Critical role of monoclinic polarization rotation in high-performance perovskite piezoelectric materials. *Phys. Rev. Lett.* **119**, 017601 (2017).
42. Liu, H. et al. Structural evidence for strong coupling between polarization rotation and lattice strain in monoclinic relaxor ferroelectrics. *Chem. Mater.* **29**, 5767–5771 (2017).
43. Acosta, M., Novak, N., Jo, W. & Rödel, J. Corrigendum to “relationship between electromechanical properties and phase diagram in the $(1-x)\text{Ba}(\text{Ti}_{0.8}\text{Zr}_{0.2})\text{O}_3\text{-}x(\text{Ba}_{0.7}\text{Ca}_{0.3})\text{TiO}_3$ lead-free piezoceramic. *Acta Mater.* **168**, 513–514 (2019).
44. Pramanick, A. et al. Stabilization of polar nanoregions in Pb-free ferroelectrics. *Phys. Rev. Lett.* **120**, 207603 (2018).
45. Leist, T. et al. Temperature dependence of the piezoelectric coefficient in $\text{BiMeO}_3\text{-PbTiO}_3$ ($\text{Me}=\text{Fe}, \text{Sc}, (\text{Mg}_{1/2}\text{Ti}_{1/2})$) ceramics. *J. Am. Ceram. Soc.* **95**, 711–715 (2012).
46. Dyadkin, V., Pattison, P., Dmitriev, V. & Chernyshov, D. A new multipurpose diffractometer PILATUS@SNBL. *J. Synchrotron Radiat.* **23**, 825–829 (2016).
47. Hammersley, A. P., Svensson, S. O., Hanfland, M., Fitch, A. N. & Häusermann, D. Two dimensional detector software: from real detector to idealised image or two-theta scan. *High. Press. Res.* **14**, 235–248 (1996).
48. Prescher, C. & Prakash, V. B. DIOPTAS: a program for reduction of two-dimensional X-ray diffraction data and data exploration. *High. Press. Res.* **35**, 223–230 (2015).
49. Yang, X., Juhas, P., Farrow, C. L. & Billinge, S. J. xPDFsuite: an end-to-end software solution for high throughput pair distribution function transformation, visualization and analysis. Preprint at <https://arxiv.org/abs/1402.3163> (2014).
50. Matthew, G. T., David, A. K., Martin, T. D., Andrew, L. G. & Qun, H. RMCProfile: reverse Monte Carlo for polycrystalline materials. *J. Phys. Condens. Matter* **19**, 335218 (2007).
51. Coelho, A. A. TOPAS and TOPAS-Academic: an optimization program integrating computer algebra and crystallographic objects written in C++. *J. Appl. Cryst.* **51**, 210–218 (2018).
52. Wang, K. et al. Temperature-insensitive $(\text{K},\text{Na})\text{NbO}_3$ -based lead-free piezoelectric ceramics. *Adv. Funct. Mater.* **23**, 4079–4086 (2013).
53. Gao, X. et al. Impact of phase structure on piezoelectric properties of textured lead-free ceramics. *Crystals* **10**, 367 (2020).

Acknowledgements

A.P. and S.V. gratefully acknowledge funding support from CityU (Projects No. 7004967, 7005121, and 9610377). A.P. acknowledges funding support from Research Grants Council of HK (Project No. 9052026 and 9043039). L.D. and A.P. would like to acknowledge the support from the Programme Hubert Curien PROCORE (No40147VF) for partial funding. F.M. and M.R.V.J. gratefully acknowledge the support by the Danish National Research Foundation (DNRF93) and the Danish Agency for Science, Technology and Innovation (DANSKATT). Affiliation with the Center for Integrated Materials Research (iMAT) at Aarhus University is gratefully acknowledged. The RMCprofile modeling was performed on resources provided by the Swedish National Infrastructure for Computing (SNIC) at LUNARC. The total scattering experiments were performed on beamline ID22 at the European Synchrotron Radiation Facility (ESRF), Grenoble, France. We are grateful to Catherine Dejoie and Andy Fitch at the ESRF for providing assistance in using beamline ID22. This research used resources of the Advanced Photon Source, a U.S. Department of Energy (DOE) Office of Science User Facility operated for the DOE Office of Science by Argonne National Laboratory under Contract No. DE-AC02-06CH11357. A.P. and L.D. acknowledges technical support at APS from Richard Spencer.

Author contributions

A.P. conceptualized the overall study. S.V., S.N., and H.C.H. synthesized the samples and performed their dielectric property measurements under guidance of A.P. S.V. and L.K.V. undertook macroscopic polarization and electrostrain measurements of the samples under guidance of J.R. V.S., and L.D. performed DIC measurements and undertook corresponding data analysis. A.P. and D.C. undertook the temperature-dependent high-resolution X-ray diffraction measurements of the powder samples. L.D. and A.P., with partial assistance from S.V. and Y.R., performed the in situ X-ray diffraction experiments under applied electric fields and undertook corresponding data analysis. F.M. and M.R.V.J. performed the measurement and RMC analysis of the X-ray total scattering data. All the authors contributed to the writing of the manuscript.

Competing interests

The authors declare no competing interests.

Additional information

Supplementary information is available for this paper at <https://doi.org/10.1038/s42005-020-00459-2>.

Correspondence and requests for materials should be addressed to A.P.

Reprints and permission information is available at <http://www.nature.com/reprints>

Publisher's note Springer Nature remains neutral with regard to jurisdictional claims in published maps and institutional affiliations.



Open Access This article is licensed under a Creative Commons Attribution 4.0 International License, which permits use, sharing, adaptation, distribution and reproduction in any medium or format, as long as you give appropriate credit to the original author(s) and the source, provide a link to the Creative Commons license, and indicate if changes were made. The images or other third party material in this article are included in the article's Creative Commons license, unless indicated otherwise in a credit line to the material. If material is not included in the article's Creative Commons license and your intended use is not permitted by statutory regulation or exceeds the permitted use, you will need to obtain permission directly from the copyright holder. To view a copy of this license, visit <http://creativecommons.org/licenses/by/4.0/>.

© The Author(s) 2020